Journal of Power Sources 184 (2008) 129–142

Contents lists available at ScienceDirect

Journal of Power Sources

journal homepage: www.elsevier.com/locate/jpowsour

Charge, mass and heat transfer interactions in solid oxide fuel cells operated with different fuel gases—A sensitivity analysis

Florian P. Nagel, Tilman J. Schildhauer*, Serge M.A. Biollaz, Samuel Stucki

Paul Scherrer Institut, Laboratory for Energy and Materials Cycles, Department General Energy, CH-5232 Villigen PSI, Switzerland

ARTICLE INFO

Article history:
Received 31 March 2008
Received in revised form 14 May 2008
Accepted 17 May 2008
Available online 23 May 2008

Keywords:
SOFC
Sensitivity analysis
Reforming kinetics
Heat and mass transfer

ABSTRACT

The interaction between charge, heat and mass transfer occurring in SOFCs is investigated applying a finite-volume-based SOFC model. The strong interactions are the consequence of the high degree of integration of different processes (chemical/electrochemical reactions, diffusion, heat and mass transfer) within SOFCs. The understanding of these interactions is a key for the future development and application of SOFCs. The investigation was conducted by means of a sensitivity analysis for two different fuel gases, where one gas features a considerable amount of methane inducing steam reforming reactions as additional disturbance factor in the energy and mass balance system of SOFCs. In order to isolate the impact of the varied model parameters and the according changes in the interactions of charge, mass and heat transfer from side effects, the sensitivity analysis was conducted at constant fuel utilization. It was found that the impact of different fuel gases on the operational conditions of SOFCs dominates geometrical and material-induced phenomena. The power output was most affected by the fuel, followed by the values for the activation polarization activation energy that reflects the employed electrode catalysts activity.

© 2008 Elsevier B.V. All rights reserved.

1. Introduction

SOFCs are expected to play an important role in future power generation due to their high efficiency. SOFCs are characterized by a high degree of integration. They can be considered as multi-functional reactors combing heat exchange, (electro-) chemical reactions (oxidation, steam reforming, and water gas shift reaction) and ionic conduction through a membrane. All these functions are strongly interrelated, making SOFCs highly complex devices. Assessing the interactions between heat and mass transfer with chemical and electrochemical reactions has become increasingly important for an effective development of SOFCs and since computational power improved, modeling has become the most important tool in this respect.

However, the complex mechanisms of SOFC electrochemistry are not yet completely understood and are therefore mostly modeled using semi-empirical correlations. This introduces several constants to the model equation system, which have to be determined experimentally in order to allow for a reliable thermal behavior and performance prediction of the SOFC in question. The relative importance of model parameters, reforming kinetics and heat transport parameters is assessed with the presented sensitivity analysis aiming at the impact on the current density distribution and local temperatures resulting in the predicted power output. The analysis is carried out considering humidified hydrogen and pre-reformed natural gas. This way the interrelations between charge, heat and mass transfer induced by electrochemical reactions can be investigated either isolated from or including the impact of steam reforming and shift reactions.

2. Model definition

The generalized finite-volume-based model was discussed in depth in [1]. Therefore only the general approach and the model extensions, which were conducted, to allow for this sensitivity analysis are discussed in this work.

The model consists of an electrochemical performance model coupled to a mass balance and an energy balance model. For a given fuel composition and operational voltage, the electrochemical performance model calculates the current density originating from hydrogen and carbon monoxide conversion according to Eqs. (1)–(3).

$$H_2 + O^{2-} \leftrightarrow H_2O + 2e^- \quad (1)$$

$$CO + O^{2-} \leftrightarrow CO_2 + 2e^- \quad (2)$$

$$O_2 + 4e^- \leftrightarrow 2O^{2-} \quad (3)$$

* Corresponding author. Tel.: +41 56 310 27 06; fax: +41 56 310 21 99.
E-mail address: tilman.schildhauer@psi.ch (T.J. Schildhauer).

0378-7753/$ – see front matter © 2008 Elsevier B.V. All rights reserved.
doi:10.1016/j.jpowsour.2008.05.044

Nomenclature

A	area [m^2]
d	diameter [m]
D	diffusion coefficient [$m^2\,s^{-1}$]
E	voltage [V]
E_{act}	activation energy for exchange current density calculation [$J\,mol^{-1}$]
F	Faraday constant [$C\,mol^{-1}$]
I	current density [$A\,m^{-2}$]
I_0	exchange current density [$A\,m^{-2}$]
K_p	equilibrium constant
l	length [m]
n	number of exchanged electrons per electrochemical reaction
n_{dot}	molar flow [$mol\,s^{-1}$]
Nu	Nusselt number
p	total or partial pressure [$N\,m^{-2}$]
P_{el}	electrical power (DC) [W]
Q_{dot}	heat flux [$W\,m^{-1}$]
r_j	reaction rate of reaction j [$mol\,s^{-1}\,m^{-1}$]
R	resistance [Ω]
R	ideal gas constant [$J\,mol^{-1}\,K^{-1}$]
T_aK	anode gas temperature [K]
T_sK	solid structure temperature [K]

Greek letters

α_{an}	convective heat exchange coefficient at anode [$W\,m^{-2}\,K^{-1}$]
α_{ca}	convective heat exchange coefficient at cathode [$W\,m^{-2}\,K^{-1}$]
β	transfer coefficient
γ	pre-exponential factor for exchange current density calculation [$A\,m^{-2}$]
δ	thickness of component [m]
ΔH	heat of reaction [$J\,mol^{-1}$]
ε	porosity of porous media
η_{act}	activation polarization voltage loss [V]
η_{diff}	diffusion polarization voltage loss [V]
η_{ohm}	ohmic voltage loss [V]
λ_s	solid structure heat conductivity coefficient [$W\,m^{-1}\,K^{-1}$]
λ_{an}	thermal conductivity of anode gas [$W\,m^{-1}\,K^{-1}$]
λ_{ca}	thermal conductivity of cathode gas [$W\,m^{-1}\,K^{-1}$]
ν_{ij}	stoichiometric coefficient of specie i in reaction j
τ	tortuosity of porous media

Subscripts and superscripts

an	anode gas channel, anode electrode
ca	cathode gas channel, cathode electrode
circ	circumferential
conv	convective
cross	cross-sectional
ed	educts
eff	effective
equiv	equivalent
hyd	hydraulic
op	operational
prod	products
SH	sensible heat
STR	steam reforming
tot	total
TPB	triple phase boundary

The voltage balance which has to be satisfied by the calculated current density values is given in the following equation:

$$E_{op} = E_{Nernst,i} - \eta_{act,t} - \eta_{diff,i} - \eta_{act,O_2} - \eta_{diff,O_2} - \eta_{ohm} \quad \text{with} \quad i = H_2, CO \tag{4}$$

In Eq. (4), η_{act} denotes the activation polarization losses, which are computed via the Butler–Volmer equation, Eq. (5).

$$I = I_0 \left[\exp\left(\beta \frac{nF\eta_{act}}{RT_sK}\right) - \exp\left(-(1-\beta)\frac{nF\eta_{act}}{RT_sK}\right)\right] \tag{5}$$

The implicit Butler–Volmer equation involves the exchange current density, I_0, which is calculated for the electrochemical reactions occurring at anode and the cathode according to Eqs. (6) and (7), respectively.

$$I_{0,an,i} = \gamma_{an,i} \left(\frac{p_i}{p}\right) \left(\frac{p_j}{p}\right)^{-0.5} \exp\left(\frac{-E_{act,an,i}}{RT_sK}\right) \quad \text{with} \quad i = H_2, CO \text{ and } j = H_2O, CO_2 \tag{6}$$

$$I_{0,ca} = \gamma_{ca} \left(\frac{p_{O_2}}{p}\right)^{0.25} \exp\left(\frac{-E_{act,ca}}{RT_sK}\right) \tag{7}$$

The ohmic voltage loss is usually the dominating effect in SOFCs. The calculation is straightforward following Ohm's law, Eq. (8).

$$\eta_{ohm} = R_{equiv} I_{tot} \tag{8}$$

Besides, the present model considers diffusion polarization losses. These account for the different partial pressures at the electrochemical reaction sites compared to the bulk gas phase. Following Fick's law, the partial pressures of the reactants at the electrochemical reactions can be computed according to the following equation:

$$p_i^{TPB} = p_i \mp \left(\frac{RT_aKI\delta_{an}\tau_{an}}{nFD_{eff}\varepsilon_{an}}\right) \quad \text{with} \quad - \text{ for } i = H_2, CO \text{ and } + \text{ for } i = H_2O, CO_2 \tag{9}$$

Knowing the bulk gas and the reaction site partial pressure values, the diffusion polarization losses are calculated via the following equation:

$$\eta_{diff,i} = \left(\frac{RT_sK}{nF}\right) \ln\left(\frac{p_i p_J^{TPB}}{p_J p_i^{TPB}}\right) \quad \text{with} \quad i = H_2, CO \text{ and } j = H_2O, CO_2 \tag{10}$$

The mass balance model requires the current density as input for the calculation of the conversion rates of the electrochemically active species, which are hydrogen, water, carbon monoxide and carbon dioxide. Further, the mass balance model includes the calculation of reaction rates for all considered homogenous and heterogeneous reactions, Eqs. (11)–(13), based on applied kinetic models or on the equilibrium approach.

$$CO + H_2O \leftrightarrow CO_2 + H_2 \tag{11}$$

$$CO_2 + H_2 \leftrightarrow CO + H_2O \tag{12}$$

$$CH_4 + H_2O \leftrightarrow CO + 3H_2 \tag{13}$$

A literature review revealed contradictory results with respect to applied kinetic models for the steam reforming reaction (STR), Eq. (13), over nickel–cermet materials. The highest discrepancies were found in the reaction order of water. Achenbach and Riensche

Table 1
Coefficients of the equilibrium constant fit correlation for the methane steam reforming reaction

Coefficient	Methane steam reforming reaction
y_0	20.45485
A_1	−294.50512
t_1	69.62891
A_2	−144.02845
t_2	182.27607
A_3	−70.17964
t_3	693.27912

found a reaction order of zero [2], Ahmed and Foger as well as Lee et al. found negative reaction orders [3,4] and Leinfelder found a positive reaction order [5]. Drescher has shown, that all these findings are correct and a result of the chosen operating conditions of the experiments, more precisely of the chosen steam-to-carbon (SC) ratio [6]. Small SC yield positive reaction orders, SC in the order of 2 yield reaction orders of zero while high SC lead to negative reaction orders of water. Drescher formulated a Langmuir–Hinshelwood type kinetic model, however for temperatures around 650 °C. All the mentioned applied kinetic models, Eqs. (15)–(18) [2,3,5,6], as well as the equilibrium approach, Eq. (14), were implemented in the developed model.

$$r_{CH_4STR,eq} = 10000.0\,\mathrm{mol\,m^{-1}\,s^{-1}}\,(\mathrm{bar}_{abs}^2)^{-1} p_{CH_4} p_{H_2O} \times \left(1 - \frac{p_{CO} p_{H_2}^3}{K_{p_{STR}} p_{CH_4} p_{H_2O}}\right) \quad (14)$$

$$r_{CH_4STR,Ach} = 4274.0\,\mathrm{mol\,m^{-1}\,s^{-1}}\,(\mathrm{bar}_{abs}^2)^{-1} p_{CH_4} \exp \times \left(\frac{-82,000\,\mathrm{J\,mol^{-1}}}{RT_sK}\right) \quad (15)$$

$$r_{CH_4STR,AhF} = 8542.0\,\mathrm{mol\,m^{-1}\,s^{-1}}\,(\mathrm{bar}_{abs}^2)^{-1} p_{CH_4}^{0.85} p_{H_2O}^{-0.35} \exp \times \left(\frac{-95,000\,\mathrm{J\,mol^{-1}}}{RT_sK}\right) \quad (16)$$

$$r_{CH_4STR,Lei} = 30.8e+10\,\mathrm{mol\,m^{-2}\,s^{-1}}\,(\mathrm{bar}_{abs}^2)^{-1} p_{CH_4} p_{H_2O} \exp \times \left(\frac{-205,000\,\mathrm{J\,mol^{-1}}}{RT_sK}\right) \quad (17)$$

$$r_{CH_4STR,Dre} = \frac{288.52\,\mathrm{mol\,m^{-2}s^{-1}}(\mathrm{bar}_{abs}^2)^{-1} p_{CH_4} p_{H_2O} \times \exp(-11,000\,\mathrm{J\,mol^{-1}}/RT_sK)}{1 + 16.0\,\mathrm{bar}_{abs}{}^{-1} p_{CH_4} + 0.143\,\mathrm{bar}_{abs}{}^{-1} p_{H_2O} \times \exp(39,000\,\mathrm{J\,mol^{-1}}/RT_sK)} \quad (18)$$

The equilibrium approach is based on the equilibrium constant the values of which were taken from [7] and fitted with Eq. (19). The fitting coefficients are given in Table 1.

$$X = y_0 + A_1 \exp\left(\frac{-T_sK}{t_1}\right) + A_2 \exp\left(\frac{-T_sK}{t_2}\right) + A_3 \exp\left(\frac{-T_sK}{t_3}\right) \quad (19)$$

The mass balance along the gas channels follows the differential equation Eq. (20).

$$\frac{dn_i}{dx} = \sum_1^j \nu_{ij} r_j \quad \text{with} \quad i = H_2, \mathrm{CO}, \text{etc. and } j = \mathrm{WGS}, \mathrm{STR}, \text{etc.} \quad (20)$$

The energy balance model serves for the calculation of the effective temperatures in the solid structure and the gas channels. It includes the calculation of the purely convective heat transfer between the gases and the solid structure as well as the conductive heat transport within the solid structure. The convective heat stream between the anode gas and the solid structure is computed following Eq. (21).

$$\dot{Q}_{conv,an} = \alpha_{an} l_{circ,an} (T_aK - T_sK) \quad \text{with} \quad \alpha_{an} = \frac{Nu\lambda_{an}}{d_{hyd,an}} \quad (21)$$

A similar expression is formulated for the convective heat exchange between the solid structure and the cathode gas, Eq. (22).

$$\dot{Q}_{conv,ca} = \alpha_{ca} l_{circ,ca} (T_sK - T_cK) \quad \text{with} \quad \alpha_{ca} = \frac{Nu\lambda_{ca}}{d_{hyd,ca}} \quad (22)$$

The convective heat terms together with all other heat source and sink terms yield the second order derivate differential equation for the solid structure energy balance including heat conduction, Eq. (23).

$$\lambda_s A_{cross} \frac{d^2 T_sK}{dx^2} = \dot{Q}_{conv,ca} - \dot{Q}_{conv,an} - \dot{Q}_{SH,ed,an} - \dot{Q}_{SH,ed,ca} - \dot{Q}_{SH,prod,an} + \Delta H_r + P_{el} \quad (23)$$

3. Sensitivity analysis

The applied methodology for the sensitivity analysis is that a single model parameter or a set of interdependent parameters is varied at once while all other parameters are held constant at the reference value. Unless otherwise stated, the varied model parameter is increased or decreased by 25% and 50% based on the respective reference value.

The operational voltage is the only real control variable of SOFCs as the fuel input flow is actually a design value which is defined by the targeted fuel utilization and the total current. Further, the input airflow follows from the targeted mean cell temperature and the maximum allowed solid temperatures. In order to conform to this, throughout the whole sensitivity analysis the fuel utilization and total current is held constant by adjusting the operational voltage. This way the impact of the varied model parameter can also be better isolated from side effects being an indirect consequence of the parameter variation. For instance, increasing the ohmic resistance with constant operational voltage yields lower fuel utilization. As a consequence of the reduced amount of electrochemical reactions, the mean cell temperature drops, causing higher ohmic losses and so on. This positive feedback effect leads to an overestimation of the impact of the increased ohmic loss. It is not always obvious what side effects could possibly distort the impact of a certain model parameter.

3.1. Reference case

The values of the varied model parameters are given in Table 2 for the reference case. The model parameter used in the prediction of diffusion losses were taken from Selimovic [8], because they represent a porous material with average properties considering the technically possible. The temperature-dependent conductivities of standard anode, electrolyte, cathode and ceramic interconnect materials were measured by Bossel who then derived the correlations proposed in [9] and used in this work. The exchange current density for the activation polarization loss calculation was computed using Eqs. (6)–(7) [10]. The required activation polarization model parameters were estimated by Costamagna by fitting the

Table 2
Electrochemical loss model input data of BMT

Model input data	Unit	Value	Source
Activation polarization			
H_2 oxidation activation energy	$J\,mol^{-1}$	120000.0	[10]
H_2 oxidation pre-exponential factor	$A\,m^{-2}$	290000000.0	
CO oxidation activation energy	$J\,mol^{-1}$	120000.0	[15]
CO oxidation pre-exponential factor	$A\,m^{-2}$	207000000.0	
O_2 reduction activation energy	$J\,mol^{-1}$	120000.0	[10]
O_2 reduction pre-exponential factor	$A\,m^{-2}$	700000000.0	
Ohmic polarization			
Electric conductivity of anode	Ω^{-1}	*T*-Dependent	[9]
Ionic conductivity of electrolyte	Ω^{-1}	*T*-Dependent	
Electric conductivity of cathode	Ω^{-1}	*T*-Dependent	
Electric conductivity of ceramic IC	Ω^{-1}	*T*-Dependent	
Diffusion polarization			
Porosity of anode	–	0.5	[8]
Tortuosity of anode	–	3.0	
Average pore diameter of anode	m	1.0E−6	
Porosity of cathode	–	0.5	
Tortuosity of cathode	–	3.0	
Average pore diameter of cathode	m	1.0E−6	

Table 4
Geometrical input data of BMT

Model input data	Unit	Value	Source
Macro-geometry of planar cell			
Flow design	–	Co- and counter-flow	[11]
Number of cells in stack	–	1	
Number of gas channels per cell	–	18	
Cell width	m	0.1	
Cell length	m	0.1	
Gas channel width	m	0.003	
Anode and cathode channel height	m	0.001	
Height of IC on anode/cathode side	m	0.00125	
Area covered by IC participating in electrochemistry	%	100.0	
Chemically active area covered by IC	%	0.0	
Micro-geometry of planar cell			
Support design	–	Electrolyte	[11]
Anode thickness	μm	50.0	
Electrolyte thickness	μm	150.0	
Cathode thickness	μm	50.0	

results obtained from the model of an electrolyte-supported planar cell to experimental voltage–current curves and temperature profiles [10]. Summing up, the employed model parameters are considered valid for the quantitative analysis presented in this work.

The sensitivity analysis is carried out for two fuel gases defined in an International Energy Agency (IEA) task aiming at the definition of a benchmark test (BMT) for SOFC models (Table 3) [11]. The IEA 1 gas allows the explicit investigation of the impact of varying model constants on the electrochemical performance. The IEA 2 gas is considered to determine the coherences when also internal reforming reactions take place. The STR reaction rates are computed via Eq. (15). The cell geometry is planar and equal to that of the IEA BMT (Table 4). The considered flow configuration is co-flow. Operational conditions for the sensitivity analysis are given in Table 5. The material property parameters used in the energy balance calculations are given in Table 6.

Table 7 summarizes the integral model response values for the reference case and both considered fuel gases. Fig. 1 depicts the predicted temperature profiles of the solid structure for the reference case and both considered fuel gases. It can be seen that at the cell inlet (*x*-axis: cell length equals zero) the temperature predicted for the fuel gas IEA 1 is approximately 65 K higher than for the fuel gas IEA 2. This can be explained with the endothermal STRs taking place with the methane containing fuel gas IEA 2. At the cell outlet (*x*-axis: cell length equals 0.1 m), the difference between the two temperature distributions is decreased to approximately 40 K. The difference between the temperature profiles of the two fuel gases is represented by the curve "Temperature difference".

3.2. Variation of activation polarization parameters

In the model, the electrochemical conversion of hydrogen and carbon monoxide were assumed to occur in parallel. Each of the conversion processes is described with an activation energy value and a pre-exponential factor. These model parameters are interdependent as, e.g. increasing only the activation energy of the hydrogen conversion leads to a compensating carbon monoxide current and vice versa. To avoid this, the activation energy values of both conversion processes are varied at once. The same applies for the pre-exponential factors.

Table 5
Operational conditions of BMT

Model input data	Unit	Value	Source
Targeted mean current density	$A\,m^{-2}$	3000.0	[11]
Targeted fuel utilization	%	85.0	
Air-to-fuel ratio	–	7.0	
Fuel gas inlet temperature	K	1173.15	
Cathode gas inlet temperature	K	1173.15	
Ambient temperature	K	293.15	
System pressure	bar_{abs}	1.01325	

Table 6
Energy balance input data of BMT

Model input data	Unit	Value	Source
Heat conductivity of anode	$W\,m^{-1}\,K^{-1}$	2.0	[11]
Heat conductivity of electrolyte		2.0	
Heat conductivity of cathode		2.0	
Heat conductivity of interconnect		2.0	
Nusselt number	–	4.0	

Table 3
Fuel and cathode gas compositions of the BMT

Specie	Unit	Fuel gas IEA 1	Fuel gas IEA 2	Cathode gas	Source
Hydrogen	vol.%	90.00	26.26	–	[11]
Carbon monoxide		–	2.94	–	
Carbon dioxide		–	4.36	–	
Water		10.00	49.34	–	
Methane		–	17.10	–	
Nitrogen		–	–	79.00	
Oxygen		–	–	21.00	

Table 7
Model response values for the reference case for IEA 1 and IEA 2 gas

Response value	Unit	IEA 1	IEA 2
Maximum solid temperature gradient	K mm^{-1}	2.2	2.0
Maximum solid temperature		1327.9	1286.9
Minimum solid temperature	K	1212.0	1146.3
Mean solid temperature		1282.7	1221.9
Operational voltage for 85% fuel utilization	V	0.683	0.624

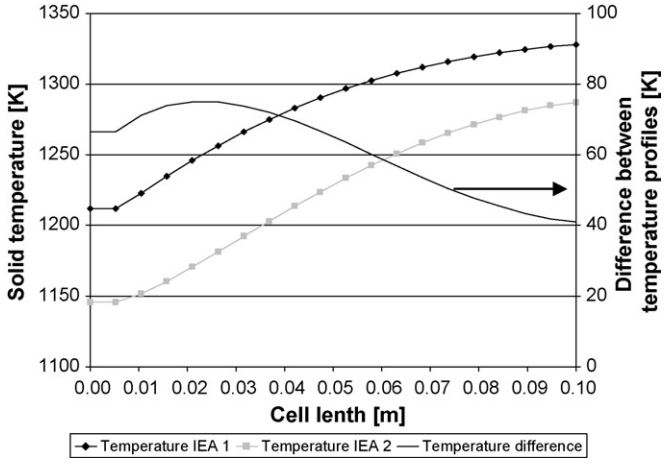

Fig. 1. Solid temperature distributions and difference for the reference case for IEA 1 and IEA 2 gas.

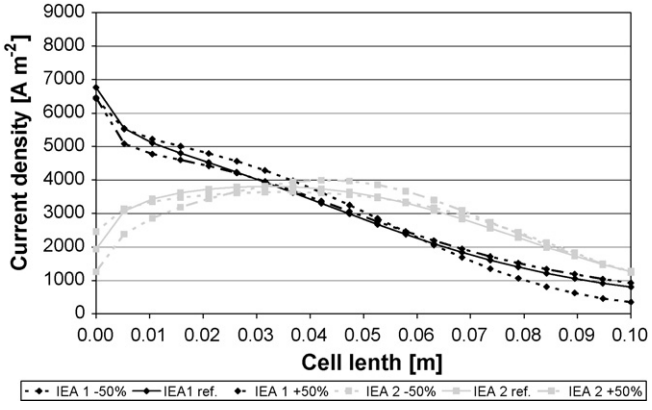

Fig. 2. Sensitivity of current density distribution towards anode activation energy.

3.2.1. Activation energy

Fig. 2 shows the sensitivity of the current density distribution towards variation of the anode activation energy. For the IEA 1 gas, the maximum current is produced at the cell inlet. This is due to the high hydrogen partial pressure of the IEA 1 gas. From thereon the current density constantly decreases along the cell length because of the ongoing fuel conversion and accordingly decreased educt partial pressure. In contrast, the IEA 2 gas yields the maximum educt partial pressures in the region where the methane STRs are complete. Hence, the current density is not constantly decreasing along the cell length, but is somewhat evenly distributed with a wide and flat peak.

Decreasing the anode activation energy means to increase the activity towards electrochemical reactions yielding higher current density values in the cell inlet region for both gases. The increased fuel consumption in the cell inlet region causes a considerable current density decrease at the cell outlet for the IEA 1 gas. However, for the IEA 2 gas the current density at the cell outlet remains constant, as the fuel consumption in the cell inlet region is dominated by the hydrogen production via STRs. This leaves more hydrogen over for the latter parts of the cell. Shortly spoken, the less hydrogen is produced within the cell via steam reforming, the more does a decrease of the activation energy lead to an increased current density at the cell inlet which is coupled to a current density decrease at the outlet.

Table 8 shows that for both fuel gases, the increase of the anode activation energy leads to an increase of the temperature extremes, the maximum temperature gradient and the mean cell temperature. This is the result of the boundary condition of keeping the fuel utilization constant, which requires higher temperatures due to the lower activity towards electrochemical reactions when the activation energy value is increased.

The operational voltage to meet the defined fuel utilization shows an asymmetric behavior. It increases only slightly for lower values and strongly decreases for higher activation energies (Fig. 3). This can be explained by the investigation of the variation intervals of the operational voltage for different activation energy values.

In the reference case, the ohmic losses are dominant; hence the value of activation losses is small. Decreasing the activation energy can at the most lead to a decrease of the activation losses close to zero. Consequently the maximum increase of the operational voltage is limited to the activation loss value of the reference case. In contrast, the activation losses become rapidly dominant by increasing the activation energy, which is part of an exponential expression. The maximum increase of the activation losses is limited by the value of the operational voltage of the reference case. Increasing the activation energy can therefore at the most lead to a decrease of the operational voltage close to zero. The different magnitude of the two described variation intervals explains the

Table 8
Model response values for different anode activation energy values for IEA 1 and IEA 2 gas

Parameter value	Maximum dT (K mm^{-1})	Cell outlet temperature (K)	Cell inlet temperature (K)	Mean cell temperature (K)	Operational voltage (V)
IEA 1 gas					
−50%	2.1	1311.6	1208.1	1274.2	0.750
−25%	2.1	1312.6	1208.4	1274.5	0.746
Reference	2.2	1327.9	1212.0	1282.7	0.683
+25%	3.0	1384.7	1223.9	1320.3	0.446
+50%	3.9	1449.5	1237.3	1364.5	0.175
IEA 2 gas					
−50%	1.7	1264.2	1142.9	1207.1	0.717
−25%	1.7	1265.8	1143.2	1208.4	0.710
Reference	2.0	1286.9	1146.3	1221.9	0.624
+25%	2.8	1345.4	1150.0	1255.2	0.376
+50%	3.7	1408.4	1153.9	1290.6	0.107

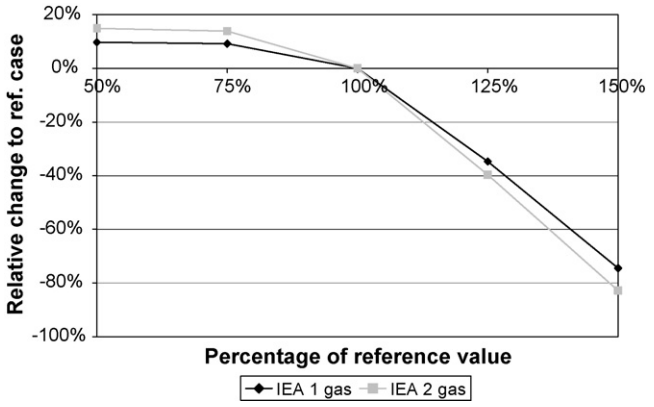

Fig. 3. Difference between the predicted power output for varying anode activation energy values.

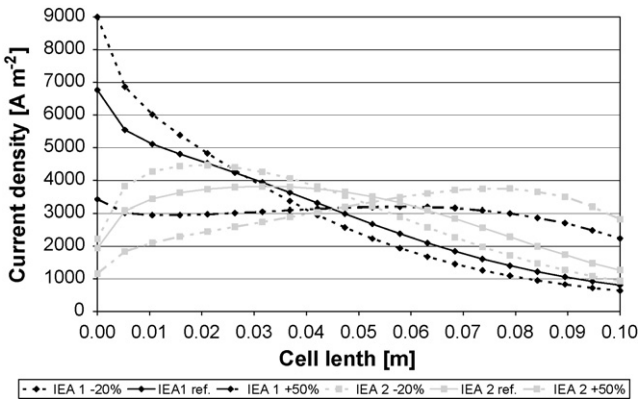

Fig. 5. Sensitivity of current density distribution towards cathode activation energy.

observed asymmetric behavior of the operational voltage for varied activation energies.

It is important to point out that SOFCs are usually not operated at voltages below 0.5 V. The predicted voltage values for increased activation energies indicate that in reality a fuel cell employing such an anode catalyst cannot reach 85% fuel utilization. For the lower activation energy values, the power output increases by a maximum of 15% and decreases by 80% for the higher values.

Fig. 4 depicts the sensitivity of the difference between the temperature profiles of the two fuel gases towards the anode activation energy. The local temperatures are strongly influenced by the locally produced power, which depends on the prevalent current density and the operational voltage, see also Table 8. For a fixed operational voltage, high current densities usually lead to high temperatures. However, endothermal reactions such as steam reforming counteract this, provided that the reaction rate is considerable.

It can be seen, that higher values of the activation energy lead to an increase of the difference between the predicted temperatures near the cell inlet and a higher reforming peak. This can be traced back to the fact that the temperature at the cell inlet for the fuel gas IEA 2 is dominated by the STR and does not change significantly by varying the activation energy. In contrast, the temperature at the cell inlet increases significantly with increasing activation energy for the IEA 1 gas. The reason for this is that the operational voltage was strongly reduced in order to meet the required overall fuel utilization. As a consequence, the amount of produced power is low

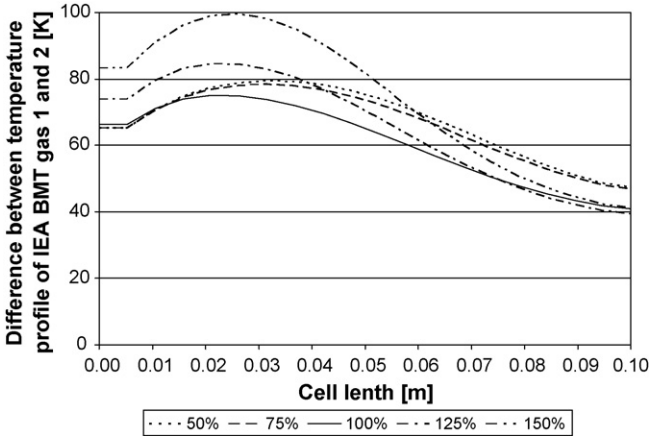

Fig. 4. Temperature difference between the predicted temperature distributions for IEA 1 and IEA 2 gas with varying anode activation energy values.

even though the current density is only slightly decreased with increasing activation energy. As less electrical power is produced from a still considerable amount of converted fuel, more sensible heat is released from the electrochemical reactions resulting in higher local temperatures.

Lowering the anode activation energy causes an increase of the temperature difference towards the cell end. Similar to the above discussed increase of the activation energy, the cell inlet temperature of the IEA 2 gas remains almost equal to the reference case. However with low activation energy values, the high amount of produced power plus the heat consumed by the endothermal steam reforming leads to a lower temperature for the IEA 2 gas at the cell outlet compared to the reference case. For the IEA 1 gas the missing steam reforming cooling is compensated to a smaller extent by low current densities at the cell outlet due to fuel depletion. Hence, the temperature difference between the two gases is increased at the cell end.

Fig. 5 depicts the sensitivity of the current density distribution towards the cathode activation energy. Note that the cathode activation energy was not decreased by more than 20% as the associated high electrochemical activity at the cell inlet for both fuel gases caused massive fuel depletion effects at the cell outlet, which resulted in numerical instability of the employed solver. For the reference case the anode activation losses are slightly higher than the cathode activation losses. By decreasing the cathode activation energy the anode activation polarization becomes dominant. As a consequence of the dependency of the anode activation polarization on the educt partial pressures, the current density increases near the cell inlet or the end of the reforming region due to the high educt partial pressures and decreases at the cell outlet due to the upstream fuel consumption. This can be observed for both investigated fuel gases.

In contrast, an increase of the cathode activation energy yields a shift from anode to cathode activation polarization as dominant activation loss mechanism. The current density then rather depends on the oxygen partial pressure than on the educt partial pressures at the anode. The oxygen partial pressure does not change significantly along the cell length due to the considerably smaller air utilization as compared to the fuel utilization. For the IEA gas 1, the high current density values at the cell inlet are inhibited by the high cathode polarization and less hydrogen is consumed. Consequently, more hydrogen is left over for conversion in the latter parts of the cell. This results in a very even current density distribution for high cathode activation energy values.

For the IEA 2 gas an increase of the cathode activation energy strongly reduces the already small current density at the cell inlet. Similar to the IEA 1 gas, more educts are left for conversion in the

Table 9
Model response values for different cathode activation energy values for IEA 1 and IEA 2 gas

Parameter value	Maximum dT (K mm^{-1})	Cell outlet temperature (K)	Cell inlet temperature (K)	Mean cell temperature (K)	Operational voltage (V)
IEA 1 gas					
−20%	2.3	1322.4	1218.8	1284.7	0.705
−10%	2.3	1323.9	1216.8	1284.2	0.699
Reference	2.2	1327.9	1212.0	1282.7	0.683
+25%	2.1	1368.1	1205.1	1290.3	0.520
+50%	2.6	1431.6	1209.1	1319.5	0.258
IEA 2 gas					
−20%	2.2	1280.2	1149.6	1225.6	0.656
−10%	2.2	1281.7	1148.3	1224.3	0.648
Reference	2.0	1286.9	1146.3	1221.9	0.624
+25%	2.4	1334.9	1143.8	1234.0	0.424
+50%	3.3	1397.3	1145.4	1258.6	0.162

latter part of the cell. However, in contrast to the IEA 1 gas, a current density peak can be observed at the cell outlet as additional hydrogen is produced via STRs and a still considerable oxygen partial pressure is present in this region. Shortly spoken, increasing the cathode activation energy yields a considerable shift of the typical steam reforming induced current density peak for hydrocarbon containing fuel gases towards the cell end. The less hydrocarbons are present in the fuel gas, the more even the current density distribution becomes.

Table 9 shows that for both fuel gases, the increase of the cathode activation energy yields an increase of the cell outlet temperature whereas the cell inlet temperature remains almost constant. This results in higher temperature gradients. The cell inlet temperature stays constant because the smaller amount of fuel conversion at the cell inlet is compensated by more released sensible heat. This is, because less electrical power is produced due to the lower operational voltage.

The impact of the cathode activation energy on the required operational voltage to maintain the defined fuel utilization is depicted in Fig. 6. Similar to the analysis of the anode activation energy, it is emphasized that operational voltages below 0.5 V are not applied in reality. With a maximum of approximately 5% power output increase, the decrease of the cathode activation energy has a smaller impact as compared to the decrease of the anode activation energy. This can be traced back to the emphasized dominating role of the anode activation polarization, which is calculated based on the reference parameters and hence inhibits a strong power output increase.

Increasing the cathode activation energy yields a power output decrease of approximately 75%. In this case, the reason for the smaller impact is that the cathode activation polarization is taking over the dominating role, weakening the impact of fuel depletion towards the cell end. Thus, the power loss, due to higher cathode activation losses, is counteracted by lower anode activation losses towards the cell end.

Fig. 7 shows the sensitivity of the difference between the temperature profiles of the two fuel gases towards the cathode activation energy. Comparing Figs. 7 and 4 it could be concluded, that the cathode activation energy has a less strong impact than the anode activation energy values on thermal behavior of the fuel cell for the two investigated fuel gases. However, the current density distributions for varied cathode activation energy values reveal another picture.

The strong reforming peak, which was discussed for higher anode activation energies, cannot be observed for the increased cathode activation energy values. Similar to the anode activation energy variation, the temperature at the cell inlet considering the IEA 2 gas is dominated by the occurring STRs and does hardly change with varying cathode activation values. Considering the IEA 1 gas with higher cathode activation energy, the temperature at the cell inlet is slightly lower then in the reference case. The reason for that is that the produced current in this region is strongly reduced compared to the reference case due to the low oxygen partial pressure at the cathode compared to the initial hydrogen partial pressure of the IEA 1 gas. However, a strong temperature decline is inhibited by the low operational voltage, which results in a fair amount of released sensible heat, which in return is sufficient to maintain the inlet temperature on a level close to the reference case. Hence, the temperature difference found at the cell inlet for increased cathode activation energy values is slightly lower than

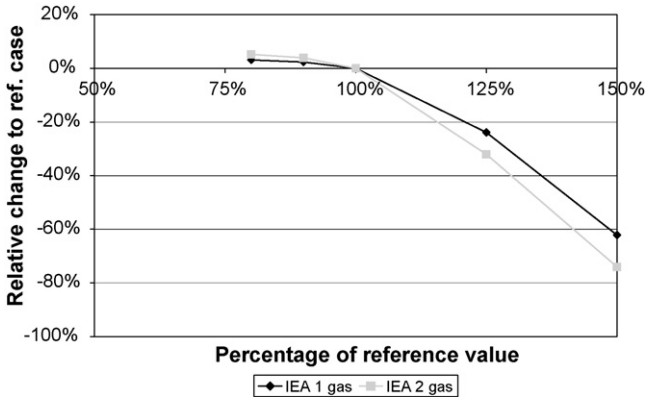

Fig. 6. Difference between the predicted power output for varying cathode activation energy values.

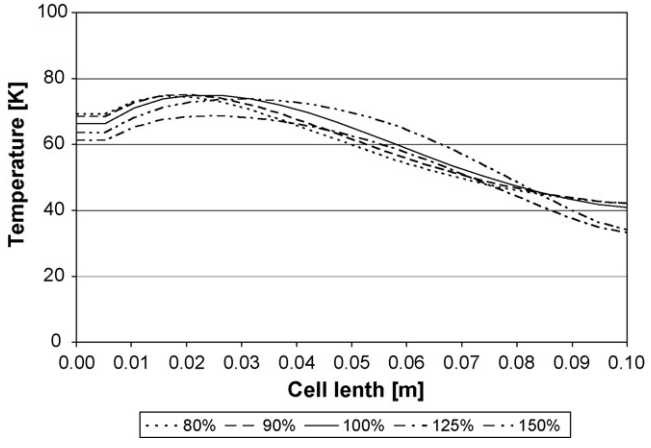

Fig. 7. Temperature difference between the predicted temperature distributions for IEA 1 and IEA 2 gas with varying cathode activation energy values.

for the reference case, which in return explains the missing steam reforming peak.

Towards the cell end, the increased cathode activation causes higher current density values due to less fuel depletion in the front parts of the cell. This can be observed for both fuel gases. However, the temperature increase towards the cell end for the IEA 2 gas is stronger due to the already discussed current density peak near the cell end. This explains the slightly lower temperature difference between the two investigated fuel gases at the cell end for higher cathode activation energy values as compared to the reference case.

As discussed for the current density distribution, decreasing the cathode activation energy puts the anode polarization into the dominating role. As the anode polarization losses are computed using the reference values, the temperature difference progression remains almost unchanged by the lowered cathode activation energy.

Concluding it can be said, that the cathode and anode activation energy values are model parameters, which have to be handled very carefully. The difference between the local temperature distributions for different fuel gases, the predicted current density distribution and power output are strongly influenced by these model parameters. In particular, the anode and cathode activation energy values influence the cell performance in a different way. Thus, it is important to know if anode or cathode activation polarization is dominant. Dominating anode activation enhances the influence of the educt partial pressure distribution leading to high fuel conversion where educt partial pressures are high and vice versa. In contrast, high cathode activation losses lead to a relatively even fuel consumption along the cell due to the almost constant oxygen partial pressures at the cathode resulting from the usually low air utilization resulting from usually excessive cooling air flows. Concerning the local temperatures, high activation losses yield a higher amount of released sensible heat partially compensating the lower amount of converted fuel and vice versa. These general rules can only be applied to a limited extent in case internal reforming reactions occur. These dominate the local temperature in any case in the region where they occur.

3.2.2. Pre-exponential factor

Within the scope of variation, the impact of the anode activation pre-exponential factor on the predicted current density distribution is small compared to the above discussed activation energy. Increased fuel consumption at the cell inlet takes place for higher pre-exponential factor values. Analogously to decreased activation energy values, the higher fuel conversion at the cell inlet yields lower current densities at the cell outlet induced by fuel depletion.

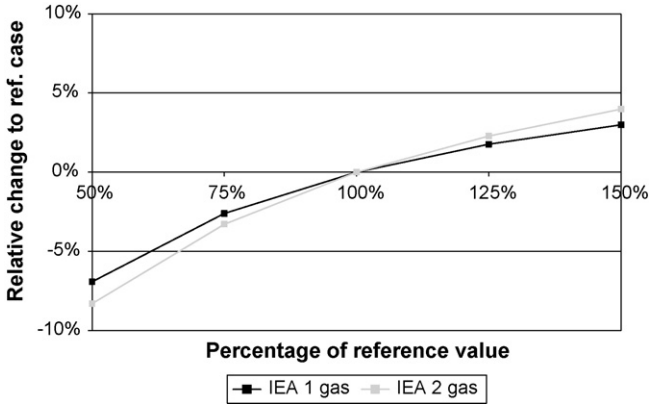

Fig. 8. Difference between the predicted power output for varying anode pre-exponential factor values.

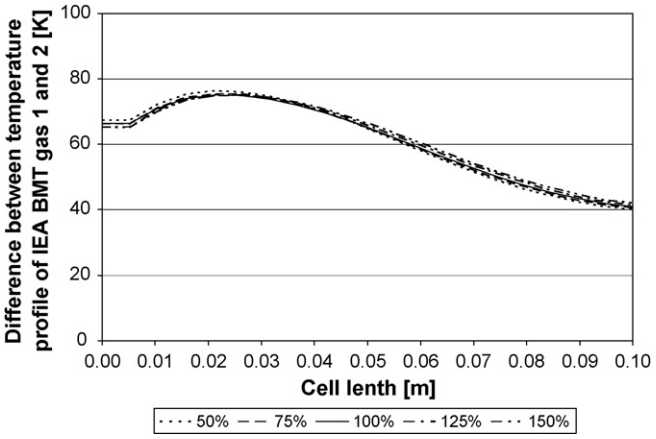

Fig. 9. Temperature difference between the predicted temperature distributions for IEA 1 and IEA 2 gas with varying anode activation pre-exponential factor values.

However, the magnitude of changes is almost negligible. The sensitivity of the predicted power for constant fuel utilization towards the anode pre-exponential factor is given in Fig. 11. In contrast to the activation energy, a decrease of the pre-exponential factor leads to decrease of power. This is because, in Eqs. (6) and (7), the exchange current density linearly depends on the pre-exponential factor whereas it depends on the multiplicative inverse of the activation energy.

For lower anode pre-exponential factor values, the power output decreases by a maximum of 8%, while it increases by a maximum of 4% for higher anode pre-exponential factor values. Similar to the variation of the activation energy values, the IEA 2 gas shows a more pronounced response. The reasons for that were discussed above.

The minor changes of the current density distribution appear for both gases to almost equal rates. Further as seen in Fig. 8, the anode pre-exponential factor has a comparably small impact on the operational voltage or predicted power, respectively, for both gases. Together this yields almost negligible changes of the temperature difference. The reason for that is that the exchange current density linearly depends on the pre-exponential factor in contrast to the exponential dependency on the activation energy value. Similar results were found in [12]. Fig. 9 depicts the sensitivity of the temperature distribution trend towards the anode pre-exponential factor.

The impact of the cathode activation pre-exponential factor on the predicted current density distribution is slightly more pronounced then for the anode activation pre-exponential factor. In contrast, the opposite is the case for the impact on the predicted power (Fig. 10). For lower cathode pre-exponential factor values, the power output decreases by a maximum of 5%, while it increases by a maximum of 2% for higher anode pre-exponential factor values. The reasons for that are the same as already discussed for the cathode activation energy variation. Higher cathode activation pre-exponential factors put the anode activation into the dominant role, while lower values lead to a more homogeneous current density distribution which equalizes fuel depletion losses at the cell ends. Fig. 11 depicts the low sensitivity of the temperature distribution trend towards the cathode pre-exponential factor.

Concluding it can be said, that the cathode and anode pre-exponential factor values are model parameters which have a minor impact on the difference between the local temperature distributions for different fuel gases, the predicted current density distribution and the predicted power output.

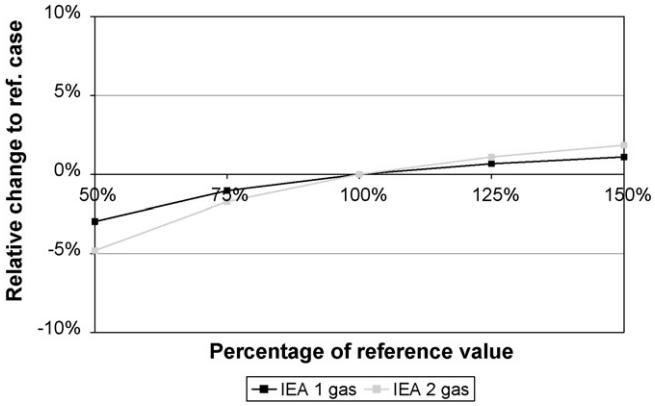

Fig. 10. Difference between the predicted power output for varying cathode pre-exponential factor values.

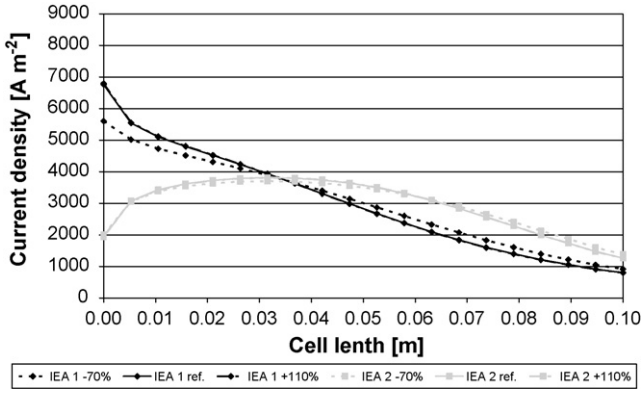

Fig. 12. Sensitivity of current density distribution towards cathode diffusion material parameters.

3.3. Variation of diffusion polarization parameters

The calculation of the diffusion losses needs as input the composition of the gas mixture and the properties of the porous media through which the specie of interest diffuses. The porous media properties include the pore diameter, which is important for Knudsen diffusion, and the porosity as well as the tortuosity. Besides the gas composition and the properties of the porous media, diffusion losses depend on temperature, the diffusion path length and local current density. The latter is causing the concentration gradient between the triple phase boundary (TPB) where the electrochemical reactions take place and the bulk gas phase. The diffusion path length has a direct influence on the concentration at the end of the diffusion path. In particular, the educt partial pressure at the TPB decreases with increasing diffusion path length. Hence, when talking about diffusion losses, one has always to keep in mind what kind of support design is investigated. For instance standard tubular cathode supported cells feature a stronger cathodic diffusion limitation than, e.g. electrolyte-supported cells due to their approximately 20 times thicker cathode. However, at low and intermediate current densities, diffusion losses are usually small or even negligible. Nevertheless, this sensitivity study has been carried out considering an electrolyte-supported planar cell in order to investigate whether the variation of the according material properties could lead to a change of these functional relationships.

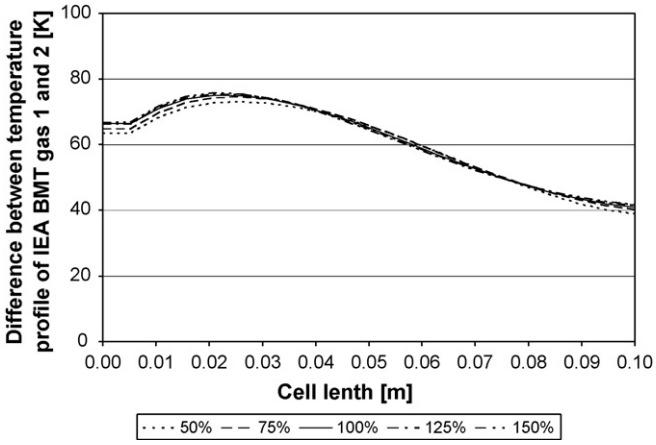

Fig. 11. Temperature difference between the predicted temperature distributions for IEA 1 and IEA 2 gas with varying cathode activation pre-exponential factor values.

The variation of the pore diameter was omitted as it simply enhances the share of Knudsen diffusion for smaller pore diameter values or reduces it for larger pore diameters. Instead, the material parameters influencing both diffusion mechanisms, i.e. the porosity and tortuosity, were varied. For the reference case the quotient of the interdependent porosity and tortuosity has the value 0.166 assuming a tortuosity of 3 and a porosity of 0.5. It was decreased by 70% to 0.05, which corresponds to a porosity of 0.25 and a tortuosity of 5 (typical values of so called dense membranes), and increased by 110% to 0.35, which corresponds to a porosity of 0.7 and a tortuosity of 2, in order to cover the full range of technically possible values.

The current density distribution did not change at all when anode material parameters were varied. With increasing porosity and decreasing tortuosity, diffusion limitations are reduced and diffusion losses become almost zero. This is however hardly noticeable as diffusion losses are already two orders of magnitude smaller than all other voltage losses in the reference case. With dense membrane like properties of the anode electrode, the diffusion of carbon monoxide is noticeably limited. However the correspondingly reduced carbon monoxide conversion is compensated by an increased hydrogen conversion, which is possible because of its very high diffusion coefficient.

In contrast, Fig. 12 gives the sensitivity of the current density distribution towards the cathode material parameters. Increasing the porosity/tortuosity quotient does not show any effect. This can be explained by the magnitude of the diffusion losses for the investigated operational conditions, which is about two orders lower than ohmic, and activation losses. However, the current density progression computed with the dense membrane values shows a considerable decrease of the current density at the cell inlet for the IEA 1 gas. This indicates that in this region, the local current density is close to the diffusion limited current density of the cathode. In these parts of a cell the high local current density results from the higher educt partial pressures as was already repeatedly discussed. For the IEA 2 gas, the same phenomenon can be observed, however less strongly pronounced.

For the increased porosity and decreased tortuosity, the power output remains constant. In contrast, assuming dense membrane properties for the anode yields a decreased power output of 0.5%. Decreasing the cathode material properties quotient results in a 2.5% power output decrease. The reason for this somewhat stronger response can be found in the smaller effective diffusion coefficient of oxygen compared to hydrogen.

Fig. 13 shows the sensitivity of the temperature distribution trend prediction towards the cathode diffusion material parameter. The parameter setting corresponding to a dense membrane leads

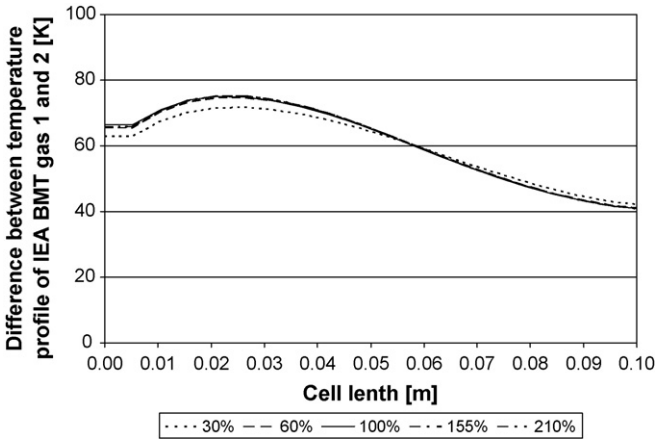

Fig. 13. Temperature difference between the predicted temperature distributions for IEA 1 and IEA 2 gas with varying cathode diffusion material parameters.

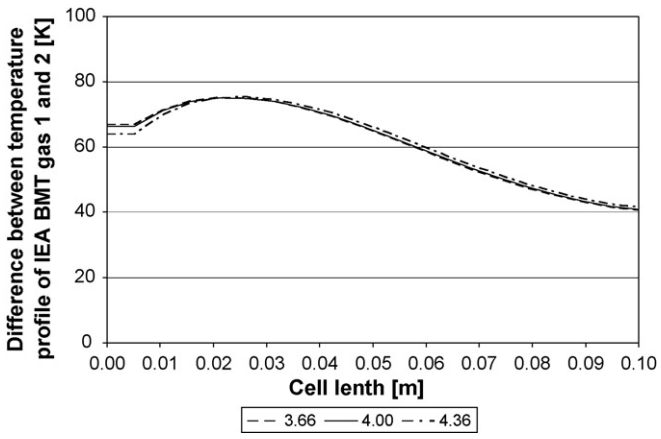

Fig. 14. Temperature difference between the predicted temperature distributions for IEA 1 and IEA 2 gas with different Nusselt numbers.

to a slightly decreased cell inlet temperature for the IEA 1 gas, as less fuel is electrochemically converted than for the reference case at the cell inlet. For the IEA 2 gas the temperature remains on the reference level due to only minor changes of the prevalent current density and the dominating STRs. In sum, the temperature difference decreases at the cell inlet for the dense membrane parameter setting.

Concluding it can be said, that for the investigated electrolyte-supported cell the anode diffusion material parameters have almost no impact on the model results. In contrast, the cathode diffusion material parameters can be set in a way, that diffusion limitations become relevant to some extent. It is important to point out that this is especially the case when other support designs with long current paths, at the cathode or anode, are investigated. Nevertheless, for the investigated support design and operating conditions the impact on the predicted power output and the thermal behavior can be neglected.

3.4. Variation of heat exchange parameters

Our model considers convective heat transport between the gases in the gas channels and the solid structure as well as conductive heat transport within the solid structure. As can be seen in Eqs. (21) and (22), the convective heat flows depend on the respective heat transfer coefficients, the heat exchange surface area and the temperature difference between the gases and the solid structure. The heat transfer coefficient is a function of the Nusselt number (*Nu*), the thermal conductivity of the considered gas mixture and the hydraulic diameter of the gas channel. In some models the Nusselt number is considered variable [13,14], however in our model, *Nu* is assumed to be constant with a value of 4. This value lies between the two special cases of heat transfer with constant heat flux, *Nu* equal to 4.36, and with constant surface temperature, *Nu* equal to 3.66, and is therefore considered to be a valid assumption [15]. The sensitivity analysis, considering both mentioned values, was carried out in order to assess the impact and the accuracy loss of the presented assumption. *Nu* values higher than 4.36 and lower than 3.66 were not considered. Lower *Nu* values are not likely to be found for the typical operating conditions of SOFCs and higher *Nu* values can be found for turbulent flow conditions, which were excluded from the developed model.

The current density distributions of both investigated gases are not changed by varying the *Nu* values. As a consequence, the change of predicted power output is in the magnitude of 0.1% and therefore negligible. Fig. 14 gives the sensitivity of the temperature distribution trend prediction towards *Nu*. The lower *Nu* value does not have a noticeable impact on the predicted temperature distribution difference for the two investigated fuel compositions. However, the increased *Nu* value yields slightly lower temperatures at the cell inlet for the IEA 1 gas and higher temperatures for the IEA 2 gas, yielding an overall smaller temperature difference at the cell inlet.

The observed opposite trends of both gases can be explained by the driving temperature difference between the solid structure and the inlet gas temperature. For the IEA 1 gas, the solid temperature is approximately 27 K higher than the inlet gas temperature. Therefore, the inlet gases are heated up by the solid structure, which in return is cooled down. Increased heat transfer therefore results in increased cooling of the cell inlet region. In contrast, the strongly endothermal STRs occurring for the IEA 2 gas at the cell inlet lead to solid structure temperatures approximately 30 K below the inlet gas temperature, i.e. the solid structure is heated up by the inflowing gases. Consequently, increased heat transfer leads to increasing solid structure temperatures, which explains the observed opposite trends.

The energy balance of the solid structure is given by Eq. (23). From the equation it can be derived that temperature of the solid structure depends on the source terms originating from chemical and electrochemical reactions, the convective heat transport between gases and solid structure and the conductive heat transport. The conductive heat transport is a function of the cross-sectional area of the solid structure through which heat is

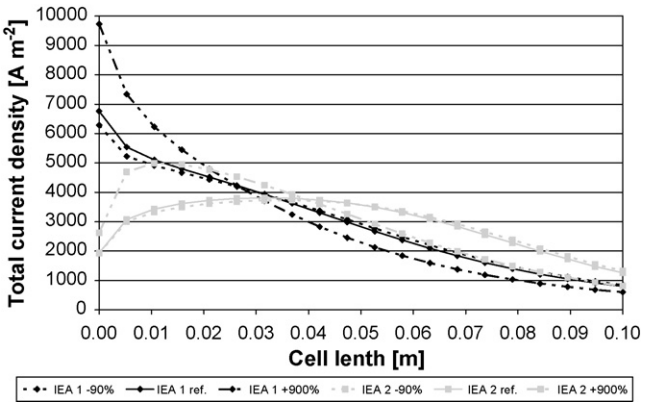

Fig. 15. Sensitivity of current density distribution towards the solid heat conductivity coefficient.

Table 10
Model response values for different solid heat conductivity coefficients for IEA 1 and IEA 2 gas

Parameter value	Maximum dT (K mm^{-1})	Cell outlet temperature (K)	Cell inlet temperature (K)	Mean cell temperature (K)	Operational voltage (V)
IEA 1 gas					
−90%	2.4	1324.9	1198.7	1274.6	0.679
−45%	2.3	1326.5	1205.8	1278.9	0.681
Reference	2.2	1327.9	1212.0	1282.7	0.683
+450%	1.8	1338.5	1257.3	1309.2	0.696
+900%	1.4	1345.2	1284.2	1324.1	0.702
IEA 2 gas					
−90%	2.0	1286.5	1141.5	1216.6	0.618
−45%	2.0	1286.5	1143.6	1219.1	0.621
Reference	2.0	1286.9	1146.3	1221.9	0.624
+450%	2.0	1296.3	1186.3	1252.7	0.647
+900%	1.7	1307.4	1223.5	1276.7	0.659

transported, the temperature difference within the solid structure and finally the effective solid's heat conductivity represented by a material parameter. For the reference case, the solid's heat conductivity coefficient (λ_S) was set to 2 W m^{-1} K^{-1}, which is a typical value for the ceramic components usually employed in SOFCs. The effect of λ_S was investigated by increasing its value to 20 W m^{-1} K^{-1}, representing the value found for high-temperature stainless steel materials which are used in some state-of-the-art SOFCs, and decreasing it to 0.2 W m^{-1} K^{-1}, which covers the case of a material with virtually no heat conduction.

Fig. 15 presents the predicted current density distribution for the investigated solid heat conductivity coefficients for IEA 1 and IEA 2 gas. Higher λ_S values yield a strong increase of the current density at the cell inlet and corresponding decrease at the cell outlet. In contrast, lower λ_S values show a minor impact on the predicted current density distribution, the power output and the thermal behavior of the modeled system considering different fuel gases. That makes sense as the reference case value of λ_S is already small. Lowering it further reduces the already small conductive heat transfer to values close to zero. Therefore, the further discussion focuses on the impact of increased λ_S values, which induce stronger changes to the energy balance of the cell.

Table 10 gives the cell temperatures and operational voltage values for varying λ_S values. Comparing the cell inlet temperature of both fuel gases for the reference case and the increased solid heat conductivity it is found that the IEA 2 gas leads to a stronger increase by approximately 5 K. In detail, the cell inlet temperature for the IEA 1 gas increases by 72 K versus 77 K for the IEA 2 gas (Fig. 16). Similar effects can be observed for the cell outlet temperatures, which increase, by 18 K for the IEA 1 gas and 20 K for the IEA 2 gas. Overall, these differences sum up to a difference of the increased mean cell temperatures of 13 K for the IEA 2 gas (54 K increase) as compared to the IEA 1 gas (41 K increase). The difference of the thermal effects for the two investigated gases is ascribed to the endothermal STRs occurring at the cell inlet for the IEA 2 gas, which represent a considerable heat sink and additional driving force for solid heat conduction. Increased λ_S values allow more heat to be transferred from the rear parts of the cell to the cell inlet, resulting into considerably higher temperature compared to the reference case for the IEA 2 gas.

In contrast, for the IEA 1 gas no endothermal reactions take place at the cell inlet. Hence, the heat transfer from the cell outlet to the cell inlet region is only driven by temperature equalization. The more pronounced mean temperature increase due to the less distinct sub-cooling region for the IEA 2 gas in return elucidates the stronger impact of the solid heat conductivity coefficient on the predicted power output which is depicted in Fig. 17.

The lower λ_S values lead to approximately 1% power output decrease while it increases by a maximum of 5.5% for higher λ_S values. In this respect, it is important to point out that all the model parameters used for the calculation of voltage losses were held constant. Keeping that in mind, the resulting dependence of the power output on the solid heat conduction coefficient is considerable. Further it gives an additional justification for the strong efforts undertaken by SOFC technology developers to use metallic materials for the interconnector plates in planar cells.

Despite the inhomogeneous current density distribution shown in Fig. 15, higher λ_S values lead to a more homogeneous temperature distribution along the cell (Fig. 16). Further, the dominating influence of the STRs on the cell inlet temperatures is weak-

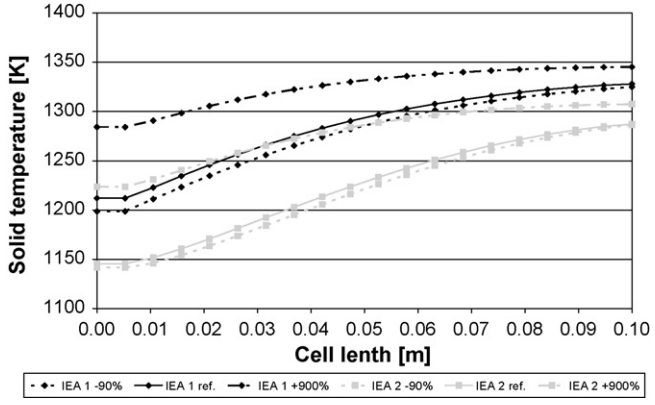

Fig. 16. Sensitivity of temperature profile towards the solid heat conductivity coefficient.

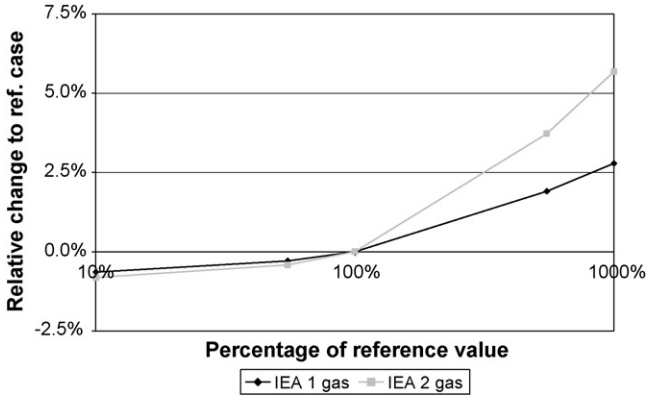

Fig. 17. Difference between the predicted power output for varying solid heat conductivity coefficients.

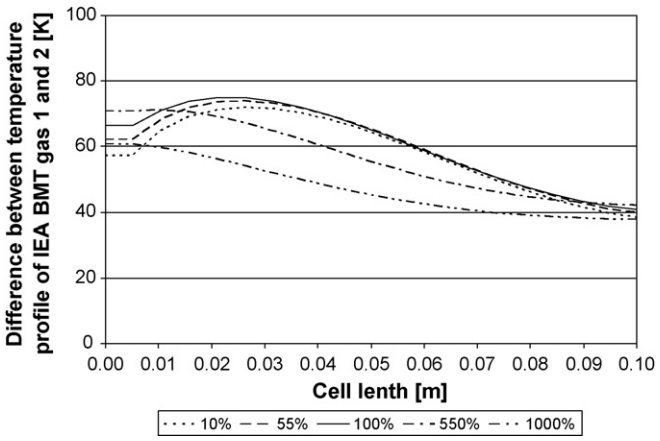

Fig. 18. Temperature difference between the predicted temperature distributions for IEA 1 and IEA 2 gas with varying solid heat conductivity values.

ened as the according heat requirements are covered by the enhanced solid heat conduction. The consequences of this are that the predicted temperature profiles for different fuel gases converge, resulting in a flattened temperature distribution without the steam reforming peak typical for the reference case (Fig. 18).

Concluding it can be said that the Nusselt number has almost no impact on the model results which justifies the according assumption and shows that the accuracy gain by holding *Nu* variable is most probably small. The heat conductivity coefficient strongly affects the predicted current density distribution and local temperature distribution. The current density tends to be less uniform for higher heat conductivity values whereas the opposite is the case for the temperature distribution. Further, for high solid heat conduction coefficients, the dominating role of the STRs occurring at the cell inlet is weakened. Hence, the differences in local temperatures between hydrocarbon containing gases and pure syngases are reduced. A considerable impact regarding the predicted power output was found despite the fact that the model parameters used for the electrochemical performance prediction were held constant at their reference value. However, the solid heat conduction is a material parameter, which can be reliably determined. Therefore is it not likely to introduce an uncontrolled uncertainty to the model results.

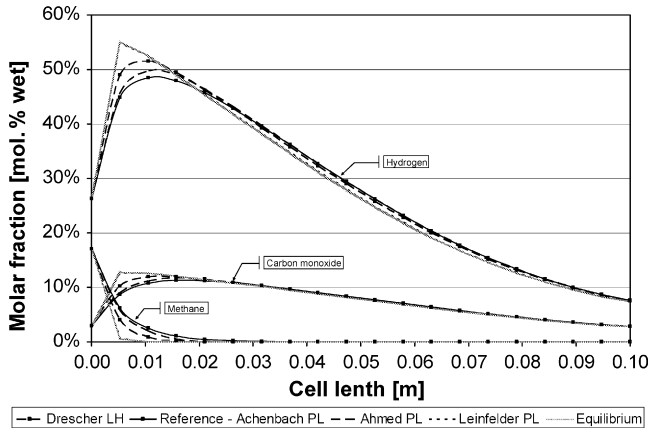

Fig. 19. Sensitivity of methane, hydrogen and carbon monoxide distribution towards STR kinetics.

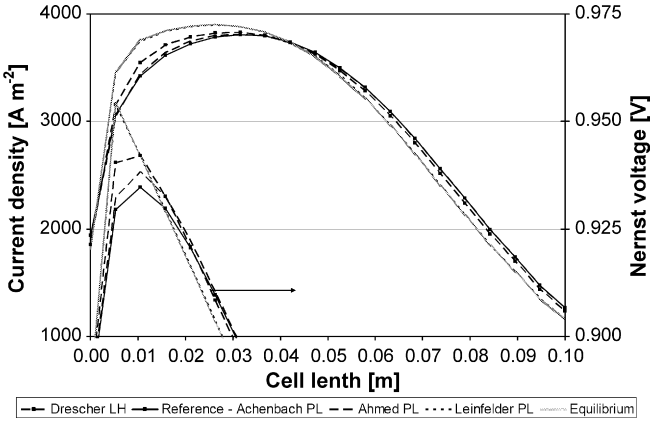

Fig. 20. Sensitivity of current density and Nernst voltage distribution towards STR kinetics.

3.5. Investigation of applied kinetics models

In SOFCs, hydrocarbons can be converted to hydrogen and carbon monoxide via STR due to the usually employed nickel-based anode material. The STR reaction rate affects the hydrogen and carbon monoxide partial pressures as well as the related Nernst voltage distribution and the temperatures where the STR reactions take place. Thus, the STR indirectly affects the electrochemical reactions occurring in SOFCs. In order to assess this impact, five different STR kinetic models, Eqs. (14)–(18), were investigated.

The reaction order of steam is controversially discussed in the literature related to STR kinetic models. The reference case of the sensitivity analysis employs the applied kinetics power law (PL) model proposed by Achenbach and Riensche [2], who found a reaction order equal to zero for steam. Ahmed and Foger also formulated a PL kinetic model for the STR [3]. In contrast to Achenbach, Ahmed found a negative reaction order for steam. Another PL model was developed by Leinfelder, who derived a first-order dependence of the STR on the steam partial pressure from his experimental data [5]. Drescher chose a Langmuir–Hinshelwood approach (LH) to describe the STR of methane over nickel cermet electrodes of SOFCs [6]. LH approaches feature variable effective reaction orders depending on the prevalent partial pressures and temperatures of the according species. The last investigated approach to predict the STR is based on the equilibrium constant of the methane STR.

Fig. 19 gives the axial distribution of methane, hydrogen and carbon monoxide for the different STR kinetic models. The Achenbach model predicts the end of the STR region at about a quarter of the

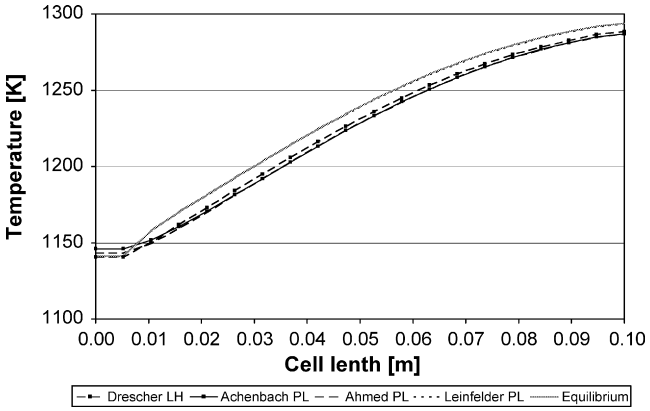

Fig. 21. Sensitivity of the temperature distribution for the IEA 2 gas towards STR kinetics.

Table 11
Model response for different methane steam reforming kinetics

Parameter value	Max. dT (K mm^{-1})	Cell outlet temperature (K)	Cell inlet temperature (K)	Mean cell temperature (K)	Operational voltage (V)
IEA 2 gas					
Reference	2.0	1286.9	1146.3	1221.9	0.624
Drescher LH	2.2	1288.4	1140.7	1223.2	0.626
Ahmed PL	2.1	1286.8	1143.2	1221.4	0.624
Leinfelder PL	3.1	1293.5	1141.0	1229.6	0.630
Equilibrium	3.2	1293.7	1141.2	1230.0	0.631

total cell length. The model proposed by Ahmed predicts slightly higher reaction rates. Therefore, STR reactions are complete after a fifth of the cell length. Drescher's LH model yields reaction rates which are about half of those obtained from the Achenbach model. The Leinfelder model results are almost congruent with the equilibrium approach, indicating that the nickel–cermet investigated by Leinfelder was highly active. Note that the considered diffusion limitation inhibits the completion of the STR reactions within the first control volume even though equilibrium is assumed. The faster the STR occurs, the higher is the corresponding hydrogen and carbon monoxide peak as the electrochemical consumption is slower than the production via the STR reactions.

Fig. 20 shows the predicted current density and Nernst voltage distribution for the different STR kinetic models. For faster STR kinetics, the current density at the cell inlet increases, yielding slightly decreased current density values at the cell outlet due to fuel depletion effects. The reason for the higher current density values at the cell inlet observed for faster STR kinetics can be found in the predicted Nernst voltage within the STR region. Higher hydrogen and carbon monoxide partial pressures yield higher Nernst voltages. Further, the Nernst voltage increases with decreasing temperatures due to the endothermal STR reactions.

Fig. 21 and Table 11 show that the cooling effect in the STR region is more pronounced for faster STR kinetics as the locally higher heat requirements cannot be fully covered via heat conduction and convection. However, towards the cell outlet, fast STR kinetics yield higher temperatures than the slow kinetics. In sum, faster STR kinetics yields higher average cell temperatures. Table 11 further gives the predicted maximum temperature gradients and operational voltages to maintain 85% fuel utilization. As a consequence of the more pronounced cooling effect and the resulting higher cell temperatures towards the cell outlet, the maximum temperature gradients increase with faster STR kinetics. The increased mean cell temperatures allow for higher operational voltage values due to less activation and ohmic voltage losses. However, the gained power output increase is in the order of 1% for the equilibrium model as compared to the reference case considering the Achenbach model.

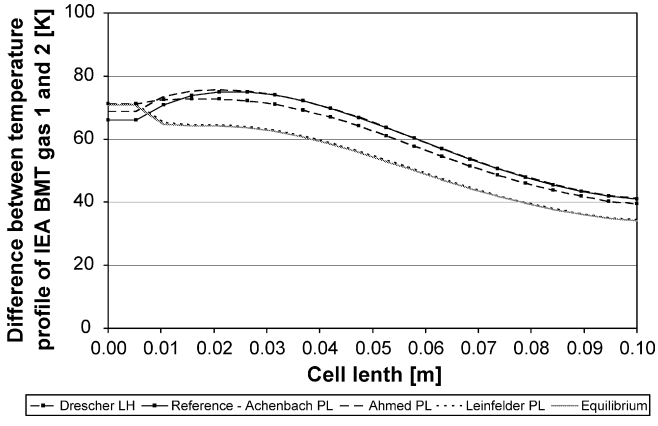

Fig. 22. Temperature difference between the predicted temperature distributions for IEA 1 and IEA 2 gas with different STR kinetic models.

Fig. 22 depicts the temperature distribution trend prediction obtained for the different STR kinetics models. The faster the STR reactions occur, the flatter and the nearer to the cell inlet is the STR peak.

Concluding is can be said, that the predicted temperature distribution depends considerably on the employed STR kinetics model. Faster STR kinetics give rise to a stronger cooling effect of the STR reactions which is counteracted by higher temperatures in the latter parts of the cell resulting from higher current density values at the cell inlet. Concerning the predicted temperature differences for different gases, the STR kinetics model has also a considerable impact. Especially the reforming peak observed for the reference case almost disappears for faster STR kinetics. In contrast, the power output is only slightly changed. The equilibrium approach, which yields almost instant methane conversion, shows power output values increased by approximately 1%.

4. Conclusions

A finite-volume-based SOFC model was used for a sensitivity analysis. The analysis was conducted to gain insights in the interaction between internal charge, heat and mass transfer processes occurring in SOFCs operated with different fuel gases.

In contrast to all other varied parameters, the activation energy values, the solid heat conduction coefficient and the chosen kinetic model for the steam reforming showed a considerable impact on the predicted temperature distributions. However, the impact of the varied parameters on the difference between the predicted temperature distributions for the investigated fuel gases was always smaller than that of the gases themselves.

With respect to the absolute power output value, only the activation energies, which reflect the activity of the employed electro-catalysts, were found to have a strong influence within the variation bandwidth. All other investigated model parameters had less then 10% variance to the reference case power output. The trends for the power output considering different fuel gases were hardly affected by the varied parameters.

It is concluded that the impact of different fuel gases on the operational conditions of SOFCs dominates geometrical- and material-induced phenomena characterized by the investigated model parameters.

References

[1] F.P. Nagel, T.J. Schildhauer, S. Biollaz, A. Wokaun, J. Power Sources, accepted for publication.
[2] E. Achenbach, E. Riensche, J. Power Sources 52 (1994) 283–288.
[3] K. Ahmed, K. Foger, Catal. Today 63 (2000) 479–487.
[4] A.L. Lee, R.F. Zabransky, W.J. Huber, Ind. Eng. Chem. Res. 29 (1990) 766–773.
[5] R. Leinfelder, Reaktionskinetische Untersuchungen zur Methan-Dampf-Reformierung und Shift-Reaktion an Anoden oxidkeramischer Brennstoffzellen, Universität Erlangen-Nürnberg, Erlangen-Nürnberg, Germany, 2004.

[6] I. Drescher, Kinetik der Methan-Dampf-Reformierung, Forschungszentrum Jülich, Jülich, Germany, 1999.
[7] E. Schmidt, Einführung in die Technische Thermodynamik, Springer, Berlin, Göttingen, Heidelberg, Germany, 1963.
[8] A. Selimovic, Modelling of Solid Oxide Fuel Cells Applied to the Analysis of Integrated Systems with Gas Turbines, Lund University, Lund, Sweden, 2002.
[9] U. Bossel, Facts & Figures, Berne, Switzerland, 1992.
[10] P. Costamagna, K. Honegger, J. Electrochem. Soc. 145 (1998) 3995–4007.
[11] E. Achenbach, Annex II: modelling and evaluation of advanced solid oxide fuel cells, IEA Program on R, D&D on advanced fuel cells: final report of activity A2, Forschungszentrum Jülich, Germany, 1996.
[12] S. Campanari, P. Iora, J. Power Sources 132 (2004) 113–126.
[13] R. Suwanwarangkul, E. Croiset, M.D. Pritzker, M.W. Fowler, P.L. Douglas, E. Entchev, J. Power Sources 154 (2006) 74–85.
[14] D. Larrain, J. Van Herle, F. Maréchal, D. Favrat, J. Power Sources 131 (2004) 304–312.
[15] C. Rechenauer, E. Achenbach, Dreidimensionale mathematische Modellierung des stationären und instationären Verhaltens oxidkeramischer Hochtemperatur-Brennstoffzellen, RWTH Aachen, Jülich, Germany, 1992.